Automated Extraction of a Depth-Defined Wave Runup Time Series From Lidar Data Using Deep Learning

Adam M. Collins, Annika O'Dea, Katherine L. Brodie, A. Spicer Bak, Tyler J. Hesser, Nicholas J. Spore, and Matthew W. Farthing

***Abstract*— Wave runup observations are key data for understanding coastal response to storms. Lidar scanners are capable of collecting swash elevation data at high spatial and temporal resolution in a range of environmental conditions. Efforts to develop automated algorithms that effectively separate returns off of the beach and the sea surface are complicated by environmental noise, thus requiring time-intensive data quality control or manual digitization. In this study, a fully convolutional neural network (FCNN) was trained and validated on 966 30-min lidar linescan time series of the beach and swash zone and tested on an additional 99 30-min linescan time series to improve the automated classification of lidar returns off of the beach and water, facilitating the extraction of a depth-defined wave runup time series. Lidar returns were classified as beach or water, and beach points at each cross-shore location were interpolated through time, creating a time-varying beach elevation surface that was used to calculate instantaneous swash depths. Runup was defined as the most landward position of 3-cm water depth through time. Overall, the runup time series determined using the manually and machine learning (ML)-digitized beach–water interface agreed well (0.02-m root-mean-square difference (RMSD) 3-cm contour location and 0.06-m RMSD 2% runup exceedance elevation R2%). The trained model was found to be robust to noise and moderate data gaps and applicable in a range of wave conditions. Results demonstrate the potential of the ML model to replace manual data processing steps and significantly reduce the time and effort required to extract the instantaneous runup location from lidar linescan time series.**

***Index Terms*— Machine learning (ML) algorithms, oceans, remote sensing.**

I. Introduction

A. Wave Runup Observations

WAVE runup, defined as the temporally varying location of the water's edge on the beach face, is a primary driver of beach and dune erosion and thus an important consideration when assessing the vulnerability of coastal infrastructure and dune systems to wave action [1], [2], [3], [4], [5], [6], [7], [8], [9]. Many storm vulnerability and hazard forecasts are predicated specifically on accurate prediction of wave runup elevations in relation to antecedent coastal morphology and infrastructure elevations [10], [11], [12]. Unfortunately, wave runup is a challenging parameter to measure due to the inherent dynamic nature of the process, particularly during storms. As a result, runup elevation datasets are limited (see [13], [14] for some recent runup observations), and scatter in runup predictions remain unexplained.

Early efforts to measure and analyze wave runup dynamics relied primarily on in situ sensors such as pressure gauges and resistance wires that collect data at either a fixed location or along a cross-shore transect [15], [16], [17]. However, in situ sensors can easily become buried or damaged during energetic conditions, limiting their use in long-term data collection efforts or during storms. To overcome these limitations, remote sensing methods (primarily based on optical imagery and lidar) have been developed, which allows for the collection of long-duration runup measurements in a wide range of wave conditions.

Optical imagery has been used in a number of studies to analyze swash processes on both reflective [18], [19] and dissipative [3], [20], [21], [22] beaches. Optical systems can be deployed over long time periods and provide information at multiple alongshore locations but only collect usable imagery during daylight hours and can suffer from detrimental visual artifacts due to weather conditions (e.g., rain and fog) or sun position (e.g., glare). Runup location is identified in optical imagery using differences in pixel intensity on a cross-shore transect, with the location of the runup time series extracted either manually [16], [21], [23] or using algorithms that employ a Radon transform [22], edge detection technique [24], or intensity threshold [25]. These algorithms generally require calibration due to changing light conditions and image intensities across the beach and water [25] and often need manual verification and correction [25], [26]. In addition, the elevation of the beach must be known and incorporated into photogrammetric equations in order to determine the accurate cross-shore position and elevation of the runup edge. This elevation information is rarely available at the necessary temporal resolution to extract runup elevations over long deployments or during storms [27], [28]. Finally, these manual digitization processes are inherently subjective, particularly

Manuscript received 30 September 2022; revised 13 December 2022; accepted 14 January 2023. Date of publication 17 February 2023; date of current version 24 February 2023. This work was supported by the U.S. Army Corps of Engineers (USACE) Coastal Field Data Collection (CFDC) Program, "Remote Sensing." The CFDC is administered at the U.S. Army Engineer Research and Development Center (ERDC), Coastal and Hydraulics Laboratory (CHL). *(Corresponding author: Adam M. Collins.)*

Adam M. Collins, Annika O'Dea, Katherine L. Brodie, A. Spicer Bak, and Nicholas J. Spore are with the Coastal and Hydraulics Laboratory, U.S. Army Engineer Research and Development Center, Duck, NC 27949 USA (e-mail: adam.collins.frf@gmail.com).

Tyler J. Hesser and Matthew W. Farthing are with the Coastal and Hydraulics Laboratory, U.S. Army Engineer Research and Development Center, Vicksburg, MS 39180 USA.

Digital Object Identifier 10.1109/TGRS.2023.3244488

during times with noisier or more ambiguous data, which introduces additional uncertainty into the extracted runup elevations and cross-shore locations. This human-based subjectivity in manual digitization processes can create differences in what is considered correct, with interlabeler agreement varying with data quality, which in some cases can result in the need for multiple human labelers of the same dataset in efforts that rely on annotated features in optical imagery of the nearshore [29], [30].

Lidar scanners have become an increasingly common tool in swash zone analyses in recent years due to their ability to collect elevation data at high spatial and temporal resolutions [9], [25], [31], [32], [33], [34], [35], [36], [37]. Swash depths can be estimated from lidar linescan time series by subtracting the sand level in the swash zone from the instantaneous elevations across the water surface [34]. Beach elevation changes can occur over short time scales (seconds to tens of minutes), with smaller changes (0–5 cm) during typical wave conditions, and larger changes (10–50 cm) during storms [16], [18], [31], [38], [39], [40]. Lidar scanners directly measure these elevation changes, allowing for a precise estimation of the instantaneous swash water depth. The estimated swash depths allow for a quantitative definition of the runup time series as the location of a specific swash depth contour and thus remove any subjectivity resulting from the manual digitization process. However, lidar data in its raw form measures the subaerial swash elevations and water surface as one continuous dataset. Data in each lidar linescan thus must be separated first into "beach" and "water" returns in order to be processed accurately. In addition, lidar data collected using systems set to "maximum sensitivity" to focus on returns off of the water surface tend to include significant noise from aerosols, spray, foam, or objects on the beach and can have increased temporal variance off of wet surfaces [37].

Various approaches to define the time-varying sand surface in the swash zone have been explored previously in the literature [9], [25], [33], [34], [35], [36], [41] for both lidar and ultrasonic altimeter observations, as both collect continuous time series of elevation, regardless of whether it is sand or water. Since the foreshore sand surface in the swash zone can evolve rapidly, defining a temporally varying bed is important for accurate analysis of these data. For short-range lidars and ultrasonic altimeters with clean signals [31], temporal variance thresholds have demonstrated skill at separating the slowly changing bed surface from the more rapidly changing sea surface. However, these algorithms have mostly been used in short-term deployments and have had to be calibrated at each site [9], [33], [41]. Vousdoukas et al. [25] used a data fusion approach where a manually calibrated algorithm was used to first digitize colocated video imagery to define the time-varying cross-shore location of the runup edge, and then, this location was used to separate lidar returns. Similarly, Fiedler et al. [34] used a manually digitized runup location to separate beach and water returns in lidar data and then calculated a mean sand surface elevation over the runup time series to define the sand elevation. It is important to note that in the case of [34], the lidar was located on a 70-m tall cliff 400 m from the swash zone and was collecting during storm conditions, and thus, noise and movement were likely a factor in the long averaging approach applied. Thus, most prior approaches using lidar data to extract runup locations have relied on some level of manual digitization, calibration, or correction, which limits workflow automation for large datasets.

B. Machine Learning Approaches to Coastal Data Processing

Machine learning (ML) approaches provide an alternative to the analytical algorithms used to extract runup location time series from remote sensing data. ML techniques have shown success at solving computer vision problems that were previously unapproachable due to complicated relationships with input features and inference target [42], [43] (and many others). ML models have been applied in a number of coastal analyses, including for the classification of rip currents [44], land cover [45], and beach states [29]; the estimation of wave heights [46], breaking [47], [48], [49], [50], and runup extent [13], [51]; the inversion of wave kinematics to solve for bathymetry [52], [53], [54], [55], [56]; and the identification of dune-toe locations from airborne lidar images [57]. Gaussian processes have also been utilized to estimate the 2% runup exceedance elevation using lidar data and bulk wave/morphology parameters (significant wave height, peak wave period, and beach slope) [58]. This analysis was possible due to a large runup dataset extracted from lidar data; however, the details of this neural network detection tool have not been published at this time [58]. These examples demonstrate the effectiveness of ML at extracting meaningful features out of image intensity or lidar point cloud data and their usefulness in the classification and interpretation of nearshore remote sensing data.

C. Objectives

The goal of this work is to develop a robust, automated analysis framework to extract wave runup elevation through time from lidar linescan data to improve the ability to utilize these unique datasets in coastal science and engineering analyses. The framework combines ML approaches with quantitative analytical runup extraction algorithms to provide a reliable and reproducible extraction of wave runup time series from repeat lidar transect observations of the beach and sea surface. The developed and tested framework will be applied within a fully automated workflow that processes continuously collected data from a shore-based lidar system deployed at the U.S. Army Engineer Research and Development Center's Field Research Facility (FRF) in Duck, NC, USA [37]. Section II details the methodology of this study, starting with an overview of the lidar data collection and preprocessing methods in Section II-A and details on a manual runup digitization process in Section II-B. The ML-based digitization process is presented in Section II-C, including details on the ML model (Section II-C1), model training and testing (Section II-C2), and the range of wave conditions during collection periods used in the training and testing (Section II-C3). The resulting comparison between the ML and manually digitized runup

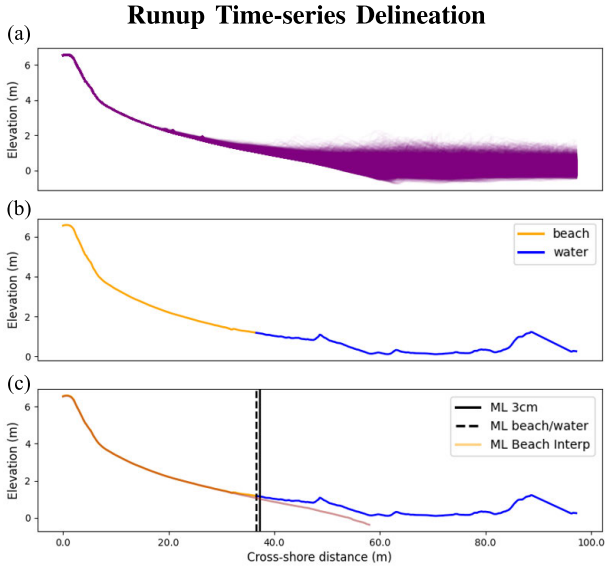

Fig. 1. Example linescan point cloud plotted as elevation (NAVD88) versus cross-shore distance from the scanner: (a) all returns over the 30-min collection period, (b) single linescan with yellow points indicating returns off the beach and blue points indicating returns off the water, and (c) same linescan with the interpolated beach shown in pink (ML Beach Interp). The ML model's predicted beach–water interface (ML beach/water) and the 3-cm water depth contour (ML 3 cm) are shown in dashed and solid lines, respectively.

extraction approaches is presented in Section III. Principal findings and conclusions are discussed in Sections IV and V, respectively.

II. Methodology

A. Lidar Data Overview

The FRF is a coastal observatory located in Duck, NC, USA, on the Atlantic coast of the United States. The facility maintains several permanently deployed in situ and remote sensors that provide coastal hydrodynamic and morphodynamic data to the broader scientific community. A fixed, continuously scanning Riegl terrestrial VZ-1000 lidar scanner (1550-nm laser) is deployed on a 4-m tower located on the foredune crest at the northern extent of the property [37]. The scanner collects a single framescan of the beach and a 30-min cross-shore linescan time series at 7 Hz each hour, producing high-density point cloud data of the elevations across the beach, swash zone, and inner surf zone [36]. The resulting data include the spatial position of each return as well as the reflectance intensity. The scanner used in this study has a high noise floor due to the sensitivity optimization parameter used during data collection. Linescans are filtered to remove objects on the beach, spray, and aerosols, and then gridded at a 10-cm resolution. The scanner has been collecting scans semicontinuously since September 2015, with collection disruptions occurring when the scanner was malfunctioning or being serviced. Processed data are publicly available to access on the Coastal and Hydraulics Laboratory's THREDDS server. Runup time series that have been manually verified are flagged but remain a minority of the total dataset. An example linescan point cloud and its subsequent delineation process can be seen in Fig. 1(a)–(c).

B. Manual Runup Time Series Delineation

The instantaneous location of the beach–water interface was identified and digitized manually across 1065 30-min linescan collection periods by visually identifying features indicative of beach or water in the lidar linescan elevation and reflectance data and derived data products through time. Several variables were used in the manual digitization process, including the elevation and reflectance intensity at each grid location, the difference between the instantaneous elevation and the minimum elevation at each grid location (referred to as Zdiff), as well as a computed variable referred to as the cumulative elevation difference (CumDiff) that estimates the likelihood from 0 to 1 of a grid cell being beach or water using the instantaneous elevation and the change in elevation at that grid cell through time. The cumulative elevation difference approach is similar to the elevation variance approached used in [33] and adapted from processing of ultrasonic altimeters [41]. Details on the cumulative elevation difference calculation can be found in [35].

The variables were visualized and interpreted during the manual digitization process by plotting each as a cross-shore transect timestack [Fig. 2(a) and (b)]. Water is identifiable in both the elevation and Zdiff timestacks as the area of changing elevation through time (x = 20–60 m, Fig. 2(b), top left and bottom right, respectively). Returns off of the water surface generally have lower reflectance values than returns off of the dry beach (Fig. 2(b), top right) and are often less dense, resulting in some gaps in coverage in the swash zone. Lidar reflectance magnitude decreases as water content increases, and thus, wet sand and water can have similarly low reflectance values. White foam, in contrast, has higher reflectivity and so appears brighter than the wet sand or water surface, making runups easier to identify when compared with rundowns. Finally, the CumDiff algorithm provides a valuable visualization of the beach–water interface, with a strong contrast in likelihood values visible between the beach and the runup tongue (Fig. 2(b), bottom left). Once the location of the beach–water interface has been visually identified at each time step, all locations onshore of the runup time series location are classified as beach, and all locations offshore of this location are classified as water (similar to the ML classification example shown in Fig. 2(d), with beach locations in purple and water locations in yellow). On average, it would take approximately 20 min of expert labor to digitize the beach–water interface for each 30-min lidar time series.

The manual digitization process relies on the digitizer's visual interpretation of the data and thus is inherently subjective, particularly during the rundown when the contrast between returns on the water and wet sand is less stark. To generate a more quantitative and consistent runup metric, the location of the 3-cm swash depth contour was extracted from the lidar data using the manually digitized beach–water interface as a constraint. Swash depths through time were calculated by subtracting a time-varying, interpolated beach elevation from the instantaneous elevation at each cross-shore location across the swash zone for each time step. The interpolated beach transect was generated by removing all data points classified during the manual digitization process

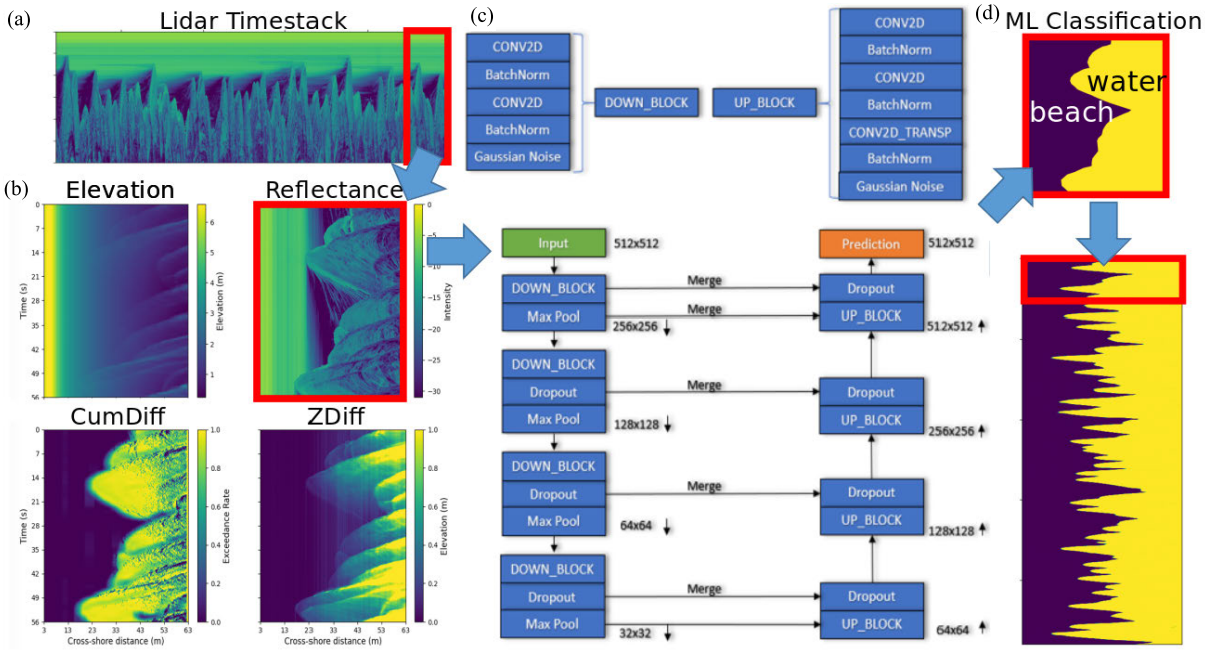

Fig. 2. Diagram of the data processing and neural network workflow: (a) example reflectance timestack showing the full time series; (b) windowed [1024 time steps by 1024 cross-shore cells, indicated with a red box in (a)] elevation, reflectance, CumDiff, and ZDiff timestack channels; (c) neural network that ingests the windowed input parameters; and (d) (Top) windowed beach–water prediction that is output from the neural network and then is merged with (bottom) other windowed sections to form the entire time series prediction. Modified from [54].

as water and then interpolating the remaining beach points through time at each cross-shore location. The interpolated beach was then smoothed using a Gaussian kernel through space and time to prevent noisy lidar returns from erroneously changing the beach profile on unrealistically short time scales. This process results in a smoothly time-varying beach elevation transect that extends down to the farthest extent of the rundown (Fig. 1(c), pink line). The interpolated beach elevation time series allows for real beach elevation changes to be included in the calculation of the swash water depths during the 30-min period. The direct measurements of beach and water surface elevation are one advantage inherent to lidar data when compared to optical imagery, which relies on a visible intensity contrast signal that does not necessarily correlate with a specific water depth contour. Once the swash depths were estimated at each time step, the first location offshore of the manually determined beach–water interface where the swash depth exceeds 3 cm was identified [solid vertical line in Fig. 1(c)]. Past lidar studies have extracted swash depth contours ranging from 3 cm [33] to 10 cm [34], based on the precision of the instrument and the experimental setup. These methods and others [9], [41] separate the beach and swash signals using a variance threshold and define the shoreline as the boundary between the bed and the swash. Because of the close proximity of the lidar scanner to the swash zone (∼60–100 m) and the precision of the instrument (∼1-cm vertical), the 3-cm contour was chosen to define the wave runup location in the present work. The term runup refers to the location of the 3-cm swash depth contour for the remainder of this article.

The precise lidar elevation data allow for a consistent and reproducible definition of the instantaneous runup location, which helps reduce the subjectivity in the manual runup extraction process. The initial beach–water interface digitization is a necessary step to constrain the swash depth contour extraction due to noisy lidar returns further up the beach that are not removed during the filtering process, including relic foam, sea spray, and pedestrians. As of July 2022, runup time series have been extracted for less than 5% of the total number of linescan time series the lidar has collected since 2015 due to the time required to manually digitize the beach–water interface.

C. ML-Based Runup Delineation

The manual runup digitization process is prohibitively slow, resulting in a growing lidar dataset that cannot be processed fully using current methods. To address this need, an ML model was developed to identify the instantaneous location of the beach–water interface in the lidar data using 966 manually digitized linescan time series. The ML model was tested to identify the beach–water interface using 99 30-min linescan collection periods over two storm events in 2016 and 2019. Consistent with the manual digitization process, the 3-cm swash depth contour was then extracted using the ML-derived beach–water interface location as a constraint. The details of the ML model development and the model training and testing are described in the following.

1) ML Model: A fully convolutional neural network (FCNN) was developed to convert the four input parameter timestacks [elevation, reflectance, Zdiff, and CumDiff, shown in Fig. 2(b)] into a beach–water classification for each grid cell (Fig. 2). The model is based on the UNET architecture [59], which was originally developed for medical image segmentation. UNET has traditionally been shown to be effective in pixelwise regression tasks in other coastal remote

sensing areas [60], [61], including our previous work on bathymetric inversion from simulated and remotely sensed nearshore images [53], [54]. For this task, downsampling and upsampling convolutional blocks with skip connections [Fig. 2(c)] are utilized to intake the four 2-D feature sets [Fig. 2(b)] created using a windowing method with no overlap and output the beach–water classification covering the same spatial and temporal extent [Fig. 2(d)]. Fig. 2(c) also details the neural network layers for predicting the beach–water interface. Downsampling and upsampling convolutional blocks are defined independently. Input data travel through a combination of convolutional blocks, dropout, batch normalization, and pooling layers. The input data first travel through the downsampled blocks shown in Fig. 2(c) (partially sourced from [53]), then through a series of four alternating convolutional and batch normalization layers, and finally a Gaussian noise layer. This output is then passed into a max-pooling layer, which downsamples the data by a factor of 2. This is repeated four times until the data are fully downsampled into a 32 × 32 grid. This downsampled output is then passed through a combination of upsampling blocks, dropout, and merge layers to create a final prediction of the beach–water classification at the original input resolution.

A knowledge-based constraint for continuity in the beach–water classification in the cross-shore is utilized in the loss function to penalize the network for producing unrealistic gradients in land–water prediction. The constraint consisted of a penalty to the network when the prediction decreased water probability in each cell when moving in the off-shore direction for each linescan transect as follows:

$$\text{Loss}_{\text{total}} = \text{Loss}_{\text{MAE}} + \begin{cases} \nabla_x(\text{prediction}) \geq 0: & 0 \\ \nabla_x(\text{prediction}) < 0: & 1 \end{cases} \quad (1)$$

where $\text{Loss}_{\text{total}}$ is the total loss, Loss_{MAE} is the mean-absolute-error loss, and $\nabla_x(\text{prediction})$ is the gradient in the predicted water probability (where a prediction of 0 indicates beach and a prediction of 1 indicates water). This loss addition is helpful for minimizing the misclassification of beach as water in the case of relic foam and other sea spray onshore of the beach–water interface during more extreme conditions such as storms. The effects of this loss are discussed in the following.

2) Model Training and Testing: The training and testing loops were designed using Tensorflow 2.0 and performed on a custom-built PC with 128 GB of RAM and a NVIDIA RTX Titan V with 24 GB of VRAM. The model takes approximately 20 h (±2 h) to converge to a minimum validation loss, and investigation showed that further training would degrade the results on the unseen test set. The model is first trained on a mean absolute error loss for five epochs and then recompiled with the modified gradient error described above for the rest of training duration. The model utilizes dropout and trainable batch normalization terms for each convolutional up and down block. Once the timestack is classified, the 3-cm swash depth contour time series is determined using the method described above. The runup time series and associated statistics are reported in the following using the derived 3-cm depth contour.

The 1065 30-min linescan time series with manually digitized beach–water interfaces were used to train, validate, and test the UNET ML model. Training and validation were performed using 966 30-min linescan time series from 2015, 2017, and 2018, with 10% of the data being set aside for validation randomly. This was done to ensure that the specific composition of the training and validation set did not affect the accuracy of the model. The test dataset consisted of 99 30-min collection periods from a Nor'easter in 2016 and Hurricane Dorian in 2019, which directly impacted the facility in Duck, NC, USA.

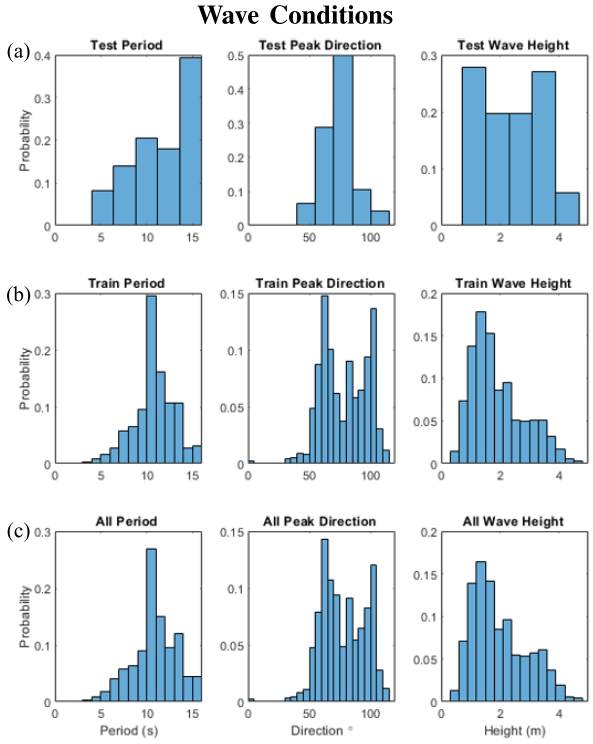

Fig. 3. Histograms of peak wave period (left column), peak wave direction (middle column), and significant wave height (right column) during linescan time series used in (a) testing dataset, (b) training dataset, and (c) combined testing and training dataset.

3) Wave Conditions: Wave conditions during collection periods used in the training and test datasets were measured using an array of pressure gauges located in approximately 8-m water depth. Histograms of the wave conditions during these collection periods are shown in Fig. 3. Many of the manually digitized 1065 linescan time series that were used to train the ML model occurred during storm events at the FRF. For this reason, the wave conditions during the collection periods used in this analysis include wave heights and periods that are larger than the average conditions at the study area. However, there is still a widespread in wave conditions during both training and testing collection periods.

D. Runup Time Series Comparisons

To assess the accuracy and consistency of the ML model in identifying the location of the beach–water interface, the locations and statistics generated from the runup time series determined using the manual digitization and the ML classification of the beach–water interface were compared. Several statistics were derived from the elevation time series, including

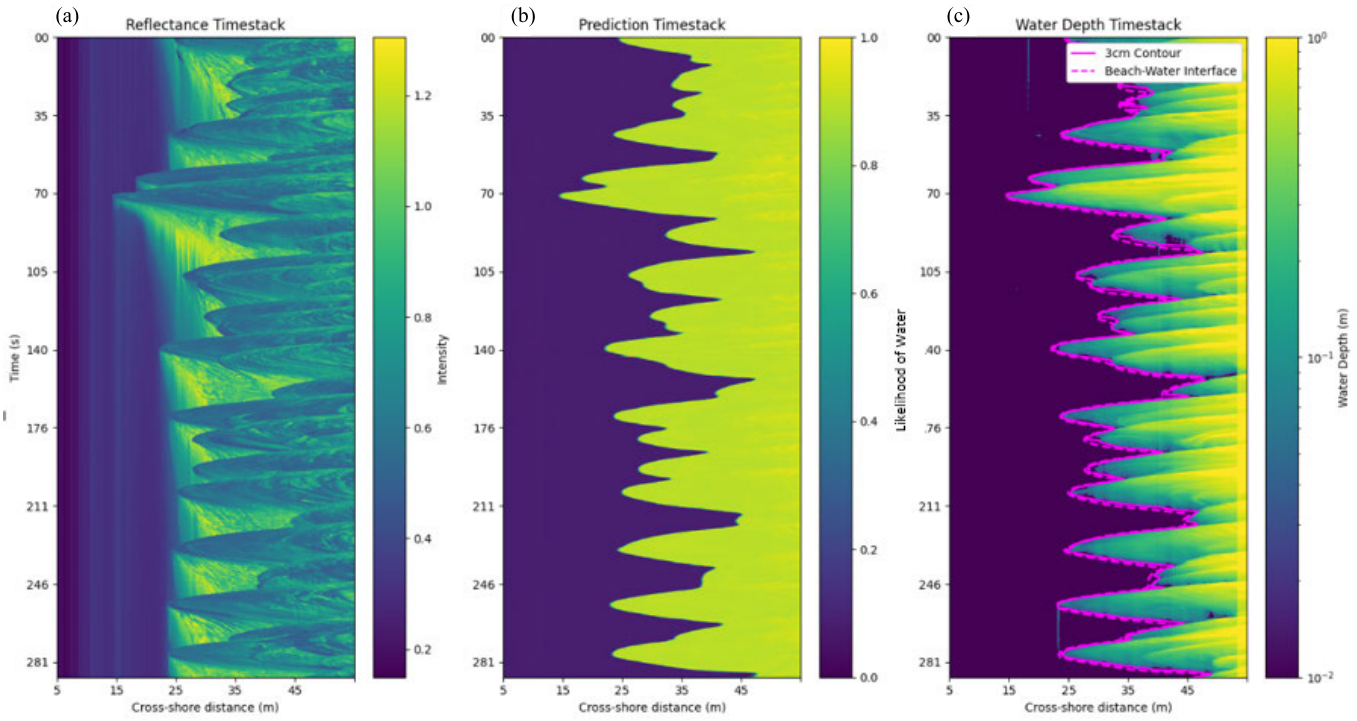

Fig. 4. Example of approximately 5 min of data from the test set on 2016-02-08-1300 UTC during a Nor'easter with significant wave height $H_s = 3.48$ m, peak wave period $T_p = 12.5$ s, and peak wave direction ($D = 71°$). (a) Reflectance, (b) ML classification (0 is beach and 1 is water), and (c) swash water depths as a function of cross-shore position and time. In (c), the ML-derived beach–water interface and final 3-cm water depth time series are shown in dashed and solid magenta lines, respectively.

the mean runup elevation (R_{mean}), the 2% runup exceedance elevation ($R_{2\%}$ runup), and the 2% rundown exceedance elevation ($R_{2\%}$ rundown). $R_{2\%}$ rundown is defined as the elevation of the lowest 2% of wave rundowns, which can be used in combination with the more commonly used $R_{2\%}$ runup to quantify the full extent of the swash.

In addition to the time series statistics, spectral statistics derived from runup frequency spectra were also calculated and compared across methods, including the total significant swash height S_{total}, the significant sea-swell swash height S_{inc}, the significant infragravity swash height S_{IG}, and the mean period T_m. Fourier analyses were conducted using the elevation of the runup time series determined from each of the two methods to generate the runup frequency spectra for each hour. From the spectra, the significant swash heights S_{total}, S_{inc}, and S_{IG} were calculated using the following equation:

$$S_{\text{total}} = 4 * \sqrt{\int_{f_1}^{f_2} \text{PSD}(f) df} \tag{2}$$

where PSD is the frequency power spectral density. For S_{total}, the spectrum was integrated over the entire frequency range. For S_{inc} and S_{IG}, the spectrum was integrated over the sea-swell ($f = 0.04$–0.5 Hz) and infragravity ($f = 0$–0.04 Hz) frequency bands, respectively. Finally, T_m was defined as the quotient of the centroidal and mean frequency from the spectral analysis.

The differences between the time series and spectral statistics determined using each of the two digitization methods were quantified by calculating the absolute difference (ML digitization—manual digitization), the root-mean-square difference (RMSD), and the bias. Due to the subjectivity inherent in the manual digitization runup methodology, the runup time series derived from the manually digitized classification are not necessarily seen as "truth." For this reason, results of the statistical comparisons are presented as differences rather than errors. This is discussed further in the following.

III. Results

Overall, the ML model was able to classify lidar returns as beach or water successfully from the four data inputs over our test set, with an example ML model input and output shown in Fig. 4(a) and (b), respectively. This separation of beach and water lidar returns enabled both the generation of the interpolated beach transects and the estimation of swash water depth transects [Fig. 4(c)]. The estimated swash depths were then used to extract the 3-cm water depth contour through time [dashed magenta line, Fig. 4(c)].

A. Example Cases

Two example cases are presented to help illustrate the beach–water interface and 3-cm swash depth contour locations determined using the different digitization methods in varying conditions (Figs. 5 and 6). In Figs. 5 and 6, the four input parameter timestacks used in the ML classification are shown on the left, with cross-shore elevation transects from four time steps shown on the right. Fig. 5 shows an example case from a Nor'easter in 2016 illustrating high-quality data. The cross-shore location of the runup is clearly visible in the four input parameter timestacks. Although there

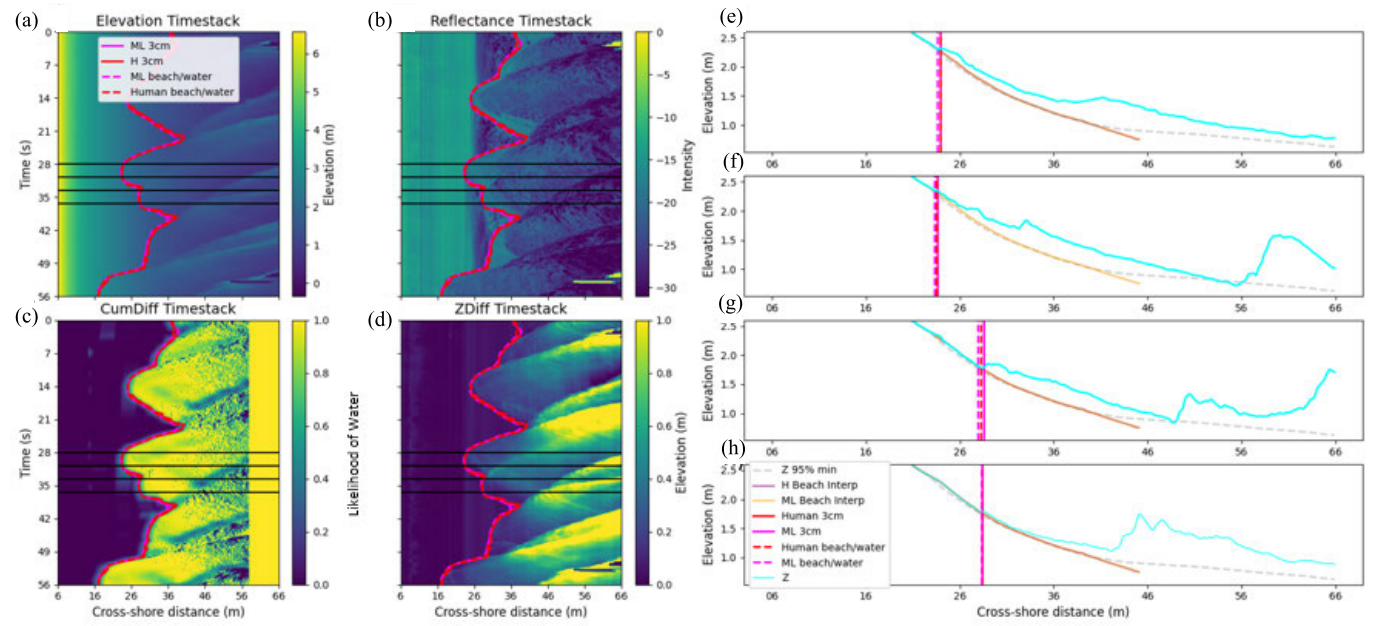

Fig. 5. Example results from a collection period on 2016-02-07-2300 used in the test set with bulk offshore wave parameters of $H_s = 4.07$ m, $T_p = 8.33$ s, and $D = 57°$. ML model inputs: (a) elevation, (b) reflectance, (c) CumDiff, and (d) Zdiff—as a function of time and cross-shore position. Dashed lines show the location of the beach–water interface determined using the ML (labeled as ML beach/water, shown in magenta) and manually digitization (human beach/water, red) methodologies, whereas solid lines show the location of the 3-cm depth contour determined using the ML (ML 3 cm, magenta) and manually digitization (H 3 cm, red) methodologies. (e)–(h) Instantaneous lidar elevation transects (Z, cyan line) as a function of cross-shore position, along with the interpolated beach elevations determined using the manually digitized (H Beach Interp, pink line) and ML-digitized (ML Beach Interp, yellow line) beach–water interface. The dotted gray line shows the elevation of the 5th percentile of lidar elevation returns for each linescan collection period. The times of the four transects in (e)–(h) are indicated with horizontal black lines in (a)–(d). The vertical dashed lines show the locations of the manually digitized (red) and ML-derived (magenta) beach–water interfaces, and the vertical solid lines show the location of the associated 3-cm depth contours (labeled as human 3 cm and ML 3 cm).

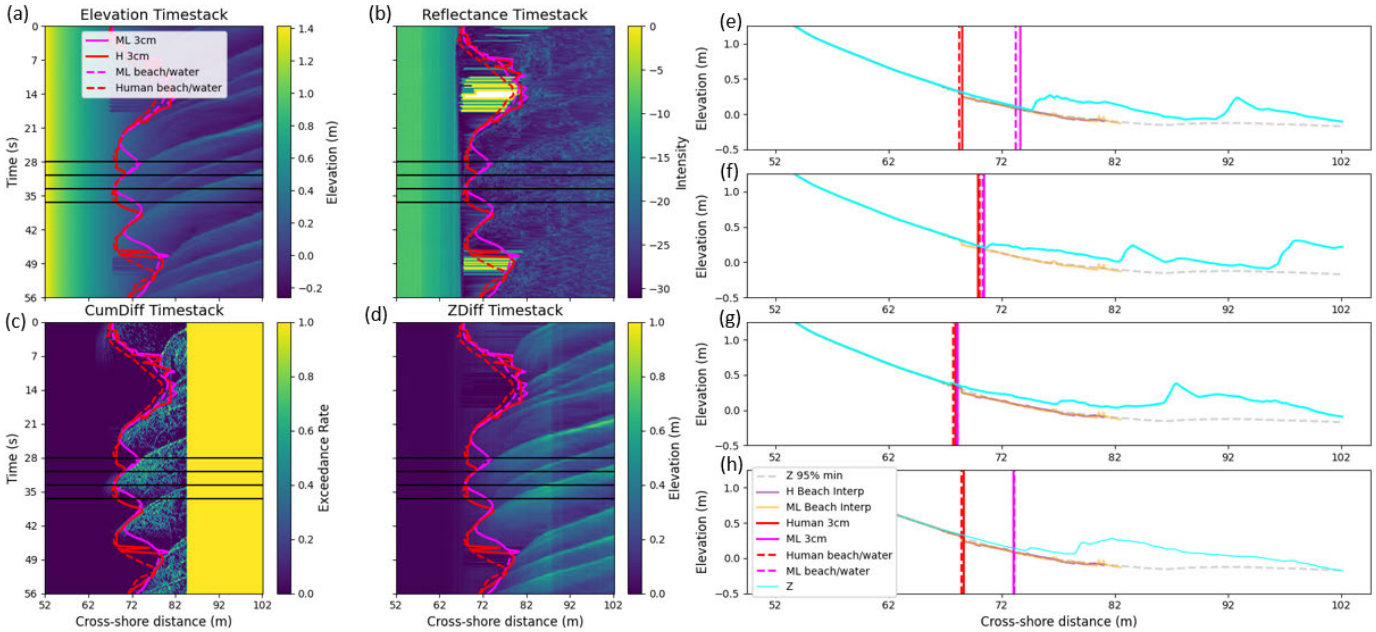

Fig. 6. Example results from a collection period on 2019-09-06-0000 near the peak of Hurricane Dorian showing times with increased environmental noise and data gaps. Offshore bulk wave parameters were $H_s = 1.90$ m, $T_p = 6.25$ s, and $D = 110°$ (see caption of Fig. 5 for plot layout).

are some small differences in the ML-digitized and manually digitized beach–water interfaces (dashed lines in all panels), there is close agreement between the 3-cm depth contour location (solid lines in all panels) determined using the two methods. The spectra calculated from the 3-cm depth contour elevations agree very well [Fig. 7(a)], with nearly identical spectral signatures (RMSD = 0.05 m^2/Hz), considering the high energies of this example (peak energy = 4.8 m^2/Hz).

Fig. 6 shows an example case from Hurricane Dorian in 2019 that contains higher levels of environmental noise, data gaps, and overall low-quality data. This time series contains examples of two data attributes that result in poor overall data

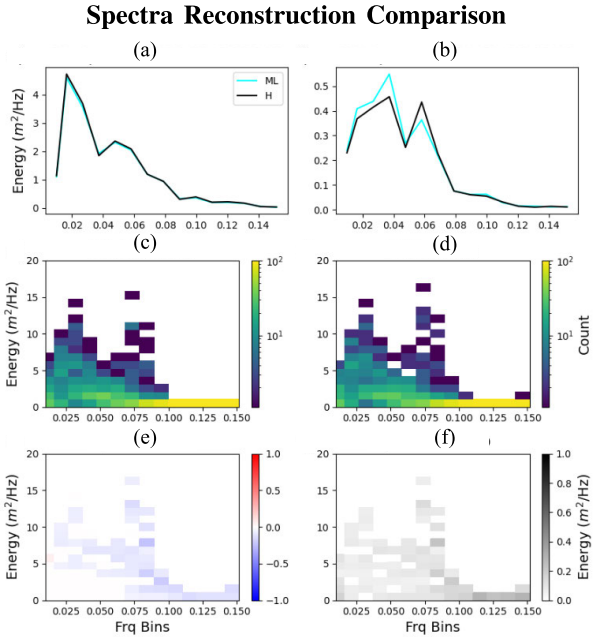

Fig. 7. (a) and (b) 1-D runup elevation spectra as a function of frequency determined using the ML- (cyan) and human-based (black) methodologies from (a) 2016-02-7-2300 (a Nor'easter) and (b) 2019-09-06-0000 (a few hours before Hurricane Dorian). (c) and (d) 2-D histograms of runup elevation spectral energy including all time series in the test dataset determined using ML- and human-based methodologies, with frequency on the x-axis, spectral energy on the y-axis, and colored by bin count; along with (e) bias and (f) RMSD between methods. The spectra shown in (a) and (b) correspond to the example cases shown in Figs. 5 and 6, respectively.

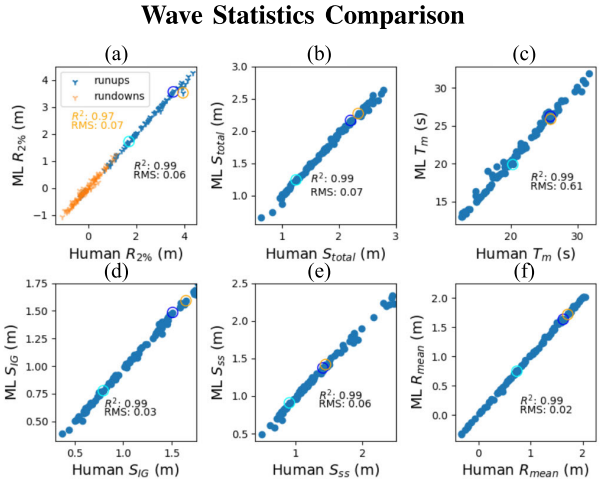

Fig. 8. Comparisons of wave runup statistics calculated using the runup elevation time series derived from the two methods: (a) $R_{2\%}$ exceedance elevation for runup (blue) and rundown (yellow), (b) total significant swash height S_{total}, (c) mean period T_m, (d) infragravity swash height S_{IG}, (e) sea-swell swash height S_{ss}, and (f) mean runup elevation R_{mean}. The example case shown in Fig. 5 is shown circled in blue. The example case shown in Fig. 6 is shown circled in cyan. The furthest outlier example in $R_{2\%}$ is shown circled in orange and is the subject of the third row of Fig. 9.

quality. First, the transect times series includes times with few or no returns in the swash zone, seen as white NaN values in the reflectance timestack [Fig. 6(b)]. This occurs primarily on the beach during rundown, when the wet sand acts as a specularly reflective surface, resulting in the reflection of the incoming laser pulse away from the lidar scanner. Second, the stormy conditions during this collection period resulted in low reflectance values in returns off the water surface, seen by comparing the reflectance timestack of Fig. 5(b) and (b). These consistent low reflectance returns during relatively large waves when significant foam is present in the surf are indicative of attenuation of the laser from rain, sea spray, and fog common during storm conditions. The poor raw data quality results in poor beach–water predictions determined using the analytical CumDiff algorithm [Fig. 6(c)]. In this example, there are large differences in beach–water interface locations determined using the manual and ML digitization methodologies [Fig. 6(e) and (h)]. At these time steps, the manually digitized beach–water interfaces (red dashed lines) are farther onshore than the ML-derived beach–water interfaces (magenta dashed lines), which results in significant differences in the associated 3-cm contour location (solid lines) and the associated runup elevation spectra [Fig. 7(b)].

B. Statistical Comparisons

The elevation of the 3-cm depth runup time series and associated swash statistics determined using the two different beach–water classification methods agreed well throughout the test dataset (Fig. 8). While only the vertical swash excursion and its derivatives are shown here, the horizontal excursion showed similar correlation. A direct comparison of the $R_{2\%}$ runup elevation determined using the two methods had an RMSD of 0.06 m and R^2 of 0.99 (Fig. 8(a), blue markers). The $R_{2\%}$ rundown elevations determined using the two methods had slightly more variability, with an RMSD of 0.07 m and R^2 of 0.97 (Fig. 8(a), orange markers). In addition, common bulk runup statistical parameters, including significant swash heights, mean runup elevation, and mean swash period, agreed well (see Fig. 8 for 1:1 plots and associated statistics).

Runup elevation spectra and spectral-based difference metrics derived from the runup elevation time series (similar to [62] and [63]) show good agreement in most scenarios (Fig. 7), with Fig. 7(b) showing an example of one of the poorest comparisons within the test dataset (the same case shown in Fig. 6). Differences in the time series result in some relatively large differences in spectral shapes and statistics (0.03 RMSD m^2/Hz and peak energy of 0.5 m^2/Hz). Spectral bias and RMSD were computed as a function of frequency and energy to investigate whether there were systematic trends to the time series differences [Fig. 7(e) and (f)]. There is close agreement between the spectral distributions [Fig. 7(c) and (d)], and however, there are some trends in the residuals [Fig. 7(e) and (f)]. The runup elevation spectra calculated using the ML-based approach are biased slightly below the runup elevation spectra calculated from the human-based approach across most of the energy-frequency space, with the highest residuals occurring during the high-frequency and high-energy conditions [Fig. 7(d)], though these instances are overall rare in the test set (Fig. 7(c) and (d) shows extremely small counts in these bands). This is consistent with the slightly increased scatter in larger significant sea-swell swash heights and lower mean swash periods visible in the 1:1 plots in Fig. 8.

IV. Discussion

While remote sensing approaches, such as video and lidar, have been utilized successfully to measure swash processes, robust and automated algorithms to extract wave runup time series can be challenging. Image-based approaches require knowledge of the beach-face elevations to generate accurate runup elevation time series, and then, the corresponding depth of the runup time series being extracted is unknown. Lidar solves many of these problems by providing elevation data of the beach and sea surface; however, accurately separating beach elevations from swash elevations can be challenging, particularly during storms when beach change can occur rapidly and environmental noise can be higher. In this work, an ML approach is demonstrated to be capable of interpreting a lidar-derived runup timestack similar to a human doing manual digitization to separate beach and swash. By inputting image timestacks of lidar-observed elevation, reflectance, and elevation variance (CumDiff and ZDiff) in both space and time, the ML model has sufficient contextual information to learn how to recognize wave runup and rundown. This is in contrast to analytical approaches, which tend to only use the information on elevation variance in time at individual cross-shore locations. The ML model can interpret and classify a 30-min lidar timestack in ∼21 s (∼3 s with a NVIDIA QUADRO RTX 5000) and a 60-fold increase (360-fold with GPU) in speed when compared to manual digitization while also removing the need for human input. Once points are classified as beach or water, a specific swash depth contour relative to a constantly updating beach can be estimated, resulting in a clearly defined and reproducible runup elevation time series. This approach allows the ML model to be used for initial image interpretation, where it should excel while retaining an objective definition of runup from the high-resolution lidar data as the 3-cm water depth contour.

A. Environmental Noise Robustness

The success of the ML model in the initial classification of beach and water data can be attributed to its ability to identify the correct beach–water interface for each time step even in the presence of environmental noise. Analytical algorithms can struggle to differentiate between increased temporal variance in elevation due to noise (such as rain, blowing foam, seaweed, dune vegetation, and beachgoers) and temporal variance in elevation due to swash runups and rundowns. For example, in Fig. 9(a) and (b), an area of high temporal variance landward of the swash zone is visible as values close to 1 (yellow) in the CumDiff timestack. The ML model, similar to the human digitizer, recognizes the parabolic runup shapes, overlooking this noise and identifying the correct beach–water interface. By including a very simple knowledge-based constraint that penalized the network having a negative gradient in beach/water prediction, the ML model is able to correctly avoid the classification of these data as water. The knowledge-based constraint for each time step also enabled the model to maintain more consistency in periods where there were gaps in the lidar data on the foreshore and swash [primarily during lower wave conditions, storms, or times when the swash zone was farther from the lidar scanner, example shown in Fig. 6(b)] than an unrestrained loss function during testing. Future work could explore more complicated approaches, which include viscous and gravitational effects to enforce a parabolic motion of wave runup through time. The ability of the model to predict successfully the beach–water interface in noisy, calm, and stormy conditions removes the need for manual data quality control, which decreases the time and human effort necessary to process the lidar data.

B. Precise Depth Contours During Erosion and Accretion

Correctly identifying the beach–water interface in each time step allows for the interpolation of beach elevations through time "beneath" runups to create a time-varying beach elevation surface in the active swash zone. This interpolated beach is an improvement over past studies (e.g., [34]) that used a mean elevation as the sand surface) because it allows for real beach change to occur over the 30-min collection period and thus enables a more precise extraction of a shallower depth contour (e.g., 3 versus 10 cm in [34]). This is particularly important during storms when significant erosion can occur in short time periods. For example, during Hurricane Dorian at the FRF, lidar observations showed that the berm completely eroded within 2.5 h, with up to 0.2 m of change within our 30-min linescan collection period in some locations (Fig. 10). The time-varying interpolated beach thus enables accurate and consistently defined runup extraction during these dynamic conditions and robustly characterizes the evolving swash morphology and hydrodynamics on process-relevant time scales (e.g., wave by wave).

Explicitly defining the runup time series by a depth contour [34] provides a consistent definition of runup, which reduces subjectivity compared to manual digitization methods using lidar or video, enables robust comparison to phase-resolved wave modeling results [8], and provides a framework to analyze the relationships between the volume of water impacting coastal structures or features and the resulting damage or change (i.e., not just a runup exceedance elevation). Subjectivity in the manual digitization of wave runup signals has been a source of potential error and scatter in runup observations used in parameterizations and annotations of other coastal processes [5], [29], [30]. Rundown can be particularly challenging to manually digitize in both video [18] and lidar data when backrushes are thin. Differences in rundown locations can have an effect on the overall variance of the runup time series (significant swash heights) as well as the mean runup, two parameters that play an important role in empirical formulations for wave runup. The value of the 3-cm contour can be seen in Fig. 9(c) and (d), where there are differences in interpretation of the beach–water interface determined by the ML and manual digitization processes (time steps 28 and 46 s). In this case, the objectivity provided by the interpolated beach and resulting swash depth contour allows both methods to agree on the location of the most seaward rundown limit during rundown, despite the original discrepancies in the definition of the beach–water interface. As evident in the similarity of the 3-cm runup time series and spectra determined using the two

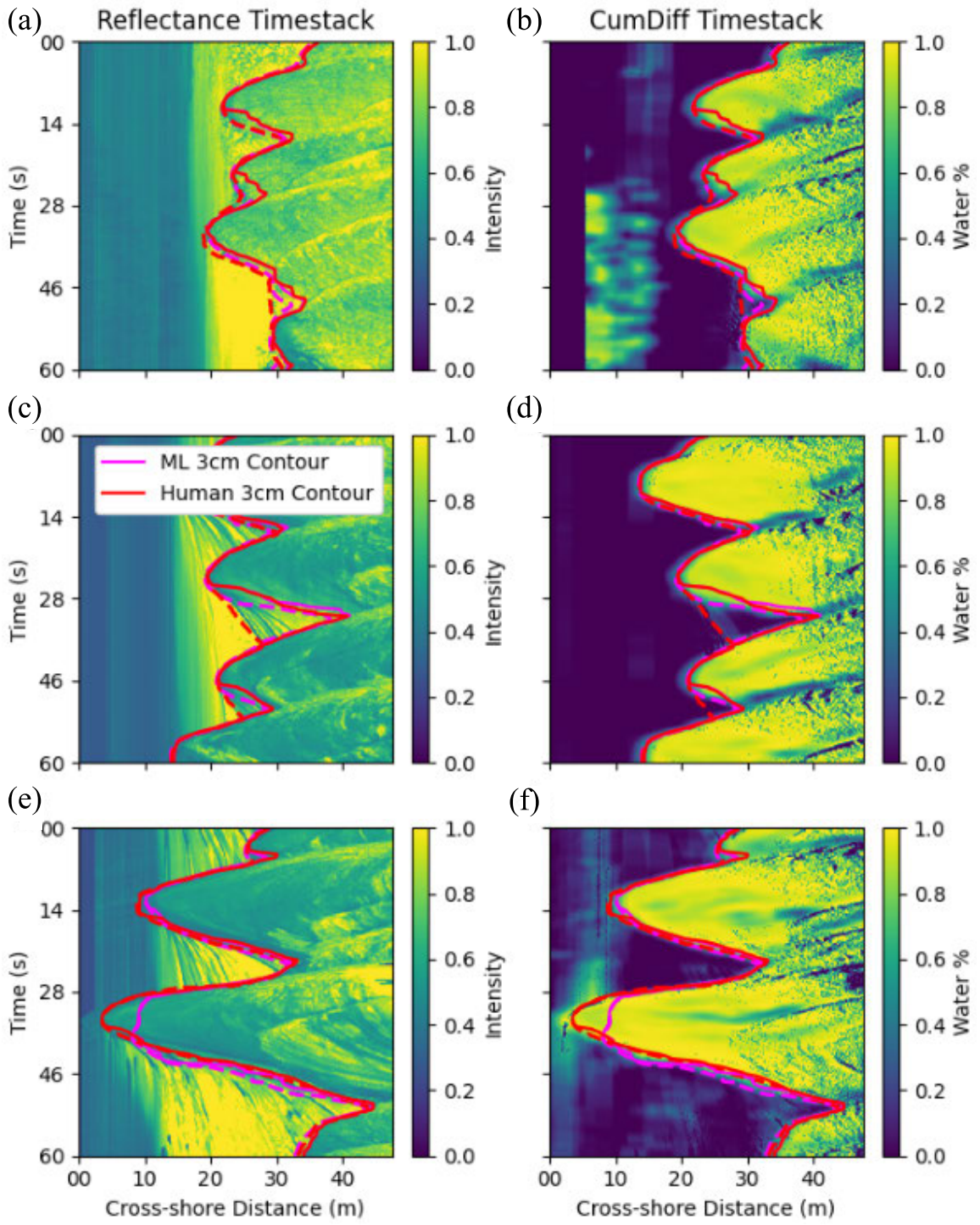

Fig. 9. (Left column) Reflectance and (Right column) CumDiff timestacks from three example collection periods during Hurricane Dorian, with the ML- (magenta) and human-derived (red) beach–water interface locations and corresponding 3-cm contour locations shown in dashed and solid lines, respectively. (a) and (b) Example case from 2016-02-08-0200, with bulk offshore wave parameters of $H_s = 4.69$ m, $T_p = 9.09$ s, and $D = 61°$. (c) and (d) Example case from 2016-02-08-1400, with bulk offshore wave parameters of $H_s = 3.17$ m, $T_p = 11.76$ s, and $D = 64°$. (e) and (f) Example case from 2019-09-06-0000, with bulk offshore wave parameters of $H_s = 3.55$ m, $T_p = 15.38$ s, and $D = 76°$.

different methodologies (Figs. 7 and 8), the approach presented here enables consistent and objective extraction of runup time series with stable distributions of variance.

C. Data Density Threshold

In general, the performance of the model was consistent across the range of wave conditions tested, as long as there were ample data observed by the lidar in the swash zone. Specifically, for the model to work well, there needed to be less than 30% of linescans throughout the 30-min collection period that has no return at the most offshore extent of the ML-estimated beach–water interface (farthest rundown limit). This threshold is a conservative estimate, based on the limited number of cases with high data gaps in the test set. It is possible that a lower threshold could be found, but this would require manual digitization of more cases with limited data

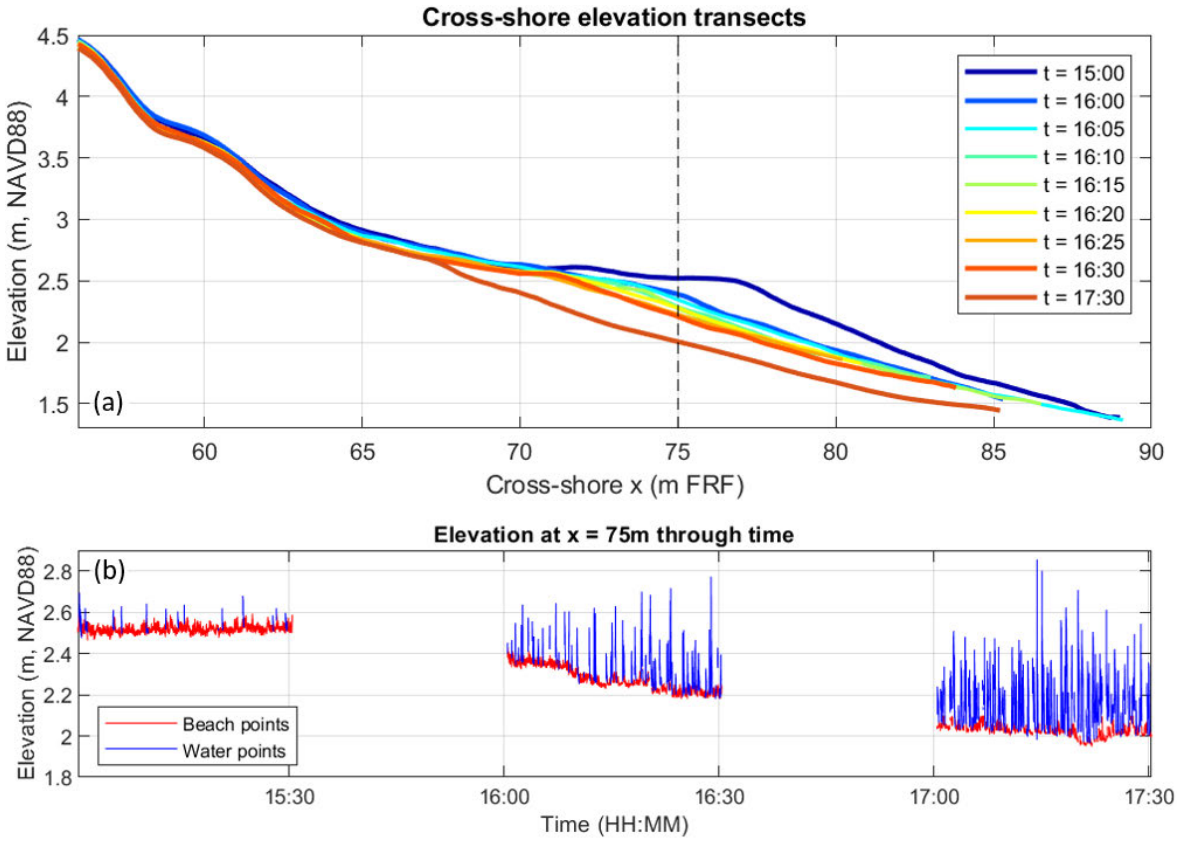

Fig. 10. (a) Lidar-derived cross-shore elevation transects over a 2.5-h period on 2019-09-06-1500 during Hurricane Dorian showing rapid beach change. (b) Lidar-derived elevation time series from $x = 75$ m over the same 2.5-h period, with beach returns in red and water returns in blue. The horizontal dashed in (a) indicates the location of the time series shown in (b).

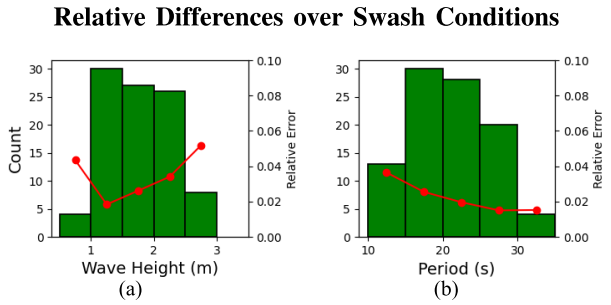

Fig. 11. Histograms of swash conditions (green bars, left y-axis) and average relative difference in R2% determined using the ML- and human-based methodologies (red lines, right y-axis) as a function of (a) significant total swash height S_{total} and (b) mean period T_m including all collection periods in the training and test datasets.

coverage to compare against. The existence of this threshold was an expected requirement, as human attempts to trace a runup contour with these datasets are also ill-advised. These conditions tend to occur during intense rain, fog, or during the smallest wave conditions when there is little breaking at the shoreline. For our test set, which included Hurricane Dorian, this threshold occurred in less than 10% of the test cases at the peak of the storm, during time periods where manual digitization of the beach–water interface was also impossible. Thus, the aforementioned data coverage requirement was implemented to remove times known to be difficult for digitization from the real-time processing of these data (>30% linescans with no return at the furthest estimated rundown extent).

When conditions met this threshold, percent differences in swash statistics derived from the runup time series determined using the ML- and human-based methodologies were less than 5.3% (see Fig. 11 for all observed S_{total} and T_m). Slightly higher percent differences in S_{total} were observed during low (<1 m) and high (>2.5 m) swash conditions, which are conditions that occurred less frequently in the test set. In addition, there are increased differences in the highest wave height bin, which could be due to increasing beach slope as you go up the beach, which results in larger elevation differences for smaller horizontal deviations in runup locations. These results are encouraging as the test dataset contains data during the near-direct impact of Hurricane Dorian. Storm conditions are some of the most valuable wave runup data to collect, and our results suggest that this methodology will be able to robustly and automatically identify the beach–water interface location during similar events.

While the ML-classification was found to be robust in a range of wave conditions, there was one notable instance in our test set, which had a slightly higher difference in $R_{2\%}$ (shown circled in orange in Fig. 8). Investigation of this time series discovered one incorrectly classified extreme runup event by the ML classification when defining the beach–water interface [Fig. 9(e) and (f)]. In this particular case, the swash uprush

ran up the dune face, creating a case not often seen during training of the model. Compounding the issue, long periods often associated with large storms and energetic swash zones create a low number (<100) of runup events during the 30-min collection period. Therefore, a misidentification of a single extreme runup event will result in a large difference in $R_{2\%}$, even though the agreement between the runup line itself during the time period is generally favorable. This issue could be improved by ongoing work to identify additional cases that have examples of dune-toe runup and adding them to the training dataset.

D. Runup Data Availability

This framework will be implemented within the FRF's real-time dune lidar processing and will be applied to historical observations, providing a wave runup dataset of over 50 000 linescan time series for the scientific and engineering communities to use. Contributions of the wave runup dataset from the full time period, the lidar system has been running, and including real-time access to future runup measurements, could have important relevance for the development of new runup models. In addition, the network model will be made available to the public so that others can adopt the methodology and use transfer learning to aid in transferring the model to other lidar systems at other locations. The following URL contains the code and model: https://github.com/FRF-Remote-Sensing/LidarRunup-ML.

V. Conclusion

In this study, an FCNN-based ML model was developed to classify beach and water returns in lidar linescan time series and trained using 966 30-min linescan time series with manually digitized beach–water interface locations. The classified data were then used to estimate swash depths and to define a runup location based on a particular swash depth contour (3 cm in this case). Overall, the resulting runup locations determined using the ML- and manually digitized beach–water interfaces compared favorably in a variety of analyses (0.02-m RMSD 3-cm contour, 0.06-m RMSD in the 2% exceedance elevation $R_{2\%}$, 0.07-m RMSD in the total swash height S_{total}, 0.61-s RMSD in the mean period T_m, 0.03-m RMSD in the infragravity swash height S_{IG}, 0.08-m RMSD in the sea-swell swash height S_{ss}, and 0.02-m RMSD in the mean runup elevation R_{mean}) over a range of wave conditions. Transforming the lidar dataset into an image-like timestack allowed for the successful leveraging of the image processing strengths of FCNNs. While the 3-cm contour was chosen for defining the wave runup location in this study, other applications could be interested in extracting other depth contours, and the swash depth estimation methods described here could be used to extract a range of depth contours in variable incident wave conditions. The quantitative runup elevations provided by the methodology could also be helpful for comparison to numerical wave models. The ML methods described should be applicable to other geographical areas and other lidar systems, and the model itself could be useful as a starting point for transfer learning to other locations and sensors to avoid the need for manual digitization of large datasets.

Acknowledgment

The authors would like to thank the operations team at the Field Research Facility for the commitment to data collection, maintenance, and processing.

References

[1] P. Ruggiero, P. D. Komar, W. G. Mcdougal, and R. A. Beach, *Extreme Water Levels, Wave Runup and Coastal Erosion*. Orlando, FL, USA: Coastal Engineering, Sep. 1996, pp. 2793–2805.

[2] J. Sallenger, "Storm impact scale for barrier islands," *J. Coastal Res.*, vol. 16, no. 3, pp. 890–895, 2000.

[3] P. Ruggiero, P. D. Komar, W. G. McDougal, J. J. Marra, and R. A. Beach, "Wave runup, extreme water levels and the erosion of properties backing beaches," *J. Coastal Res.*, vol. 17, no. 2, pp. 407–419, 2001.

[4] B. Elfrink and T. Baldock, "Hydrodynamics and sediment transport in the swash zone: A review and perspectives," *Coast. Eng.*, vol. 45, nos. 3–4, pp. 149–167, May 2002.

[5] H. F. Stockdon, R. A. Holman, P. A. Howd, and A. H. Sallenger, "Empirical parameterization of setup, swash, and runup," *Coastal Eng.*, vol. 53, no. 7, pp. 573–588, May 2006.

[6] K. D. Splinter, D. Strauss, and R. B. Tomlinson, "Can we reliably estimate dune erosion without knowing pre-storm bathymetry?" in *Proc. 20th Australas. Coasts Ports Conf.*, 2011, pp. 650–655.

[7] N. G. Plant and H. F. Stockdon, "Probabilistic prediction of barrier-island response to hurricanes," *J. Geophys. Res., Earth Surf.*, vol. 117, no. 3, pp. 1–17, 2012.

[8] J. W. Fiedler, P. B. Smit, K. L. Brodie, J. McNinch, and R. T. Guza, "Numerical modeling of wave runup on steep and mildly sloping natural beaches," *Coastal Eng.*, vol. 131, pp. 106–113, Jan. 2018, doi: 10.1016/j.coastaleng.2017.09.004.

[9] M. S. Phillips, C. E. Blenkinsopp, K. D. Splinter, M. D. Harley, and I. L. Turner, "Modes of berm and beachface recovery following storm reset: Observations using a continuously scanning LiDAR," *J. Geophys. Res., Earth Surf.*, vol. 124, no. 3, pp. 720–736, Mar. 2019.

[10] A. L. Aretxabaleta, K. S. Doran, J. W. Long, L. H. Erikson, and C. D. Storlazzi, "Toward a national coastal hazard forecast of total water levels," in *Proc. 9th Int. Conf.*, 2019, pp. 1373–1384.

[11] M. A. Merrifield et al., "An early warning system for wave-driven coastal flooding at Imperial Beach, CA," *Natural Hazards*, vol. 108, no. 3, pp. 2591–2612, 2021.

[12] C. K. Leaman, M. D. Harley, K. D. Splinter, M. C. Thran, M. A. Kinsela, and I. L. Turner, "A storm hazard matrix combining coastal flooding and beach erosion," *Coastal Eng.*, vol. 170, Dec. 2021, Art. no. 104001.

[13] H. E. Power, B. Gharabaghi, H. Bonakdari, B. Robertson, A. L. Atkinson, and T. E. Baldock, "Prediction of wave runup on beaches using gene-expression programming and empirical relationships," *Coastal Eng.*, vol. 144, pp. 47–61, Feb. 2019.

[14] P. Gomes da Silva, G. Coco, R. Garnier, and A. H. F. Klein, "On the prediction of runup, setup and swash on beaches," *Earth-Sci. Rev.*, vol. 204, May 2020, Art. no. 103148. [Online]. Available: https://www.sciencedirect.com/science/article/pii/S0012825219306828

[15] R. T. Guza, E. B. Thornton, and R. A. Holman, "Swash on steep and shallow beaches," in *Proc. Coastal Eng.*, Nov. 1985, pp. 708–723.

[16] K. T. Holland, B. Raubenheimer, R. T. Guza, and R. A. Holman, "Runup kinematics on a natural beach," *J. Geophys. Res., Oceans*, vol. 100, no. C3, pp. 4985–4993, 1995.

[17] B. Raubenheimer, R. Guza, S. Elgar, and N. Kobayashi, "Swash on a gently sloping beach," *J. Geophys. Res., Oceans*, vol. 100, no. C5, pp. 8751–8760, 1995.

[18] R. A. Holman and A. H. Sallenger Jr., "Setup and swash on a natural beach," *J. Geophys. Res., Oceans*, vol. 90, no. C1, pp. 945–953, 1985, doi: 10.1029/JC090iC01p00945.

[19] K. T. Holland and R. A. Holman, "Wavenumber-frequency structure of infragravity swash motions," *J. Geophys. Res., Oceans*, vol. 104, no. C6, pp. 13479–13488, Jun. 1999.

[20] B. G. Ruessink, M. G. Kleinhans, and P. G. L. van den Beukel, "Observations of swash under highly dissipative conditions," *J. Geophys. Res., Oceans*, vol. 103, no. C2, pp. 3111–3118, Feb. 1998.

[21] R. M. C. Guedes, K. R. Bryan, and G. Coco, "Observations of wave energy fluxes and swash motions on a low-sloping, dissipative beach," *J. Geophys. Res., Oceans*, vol. 118, no. 7, pp. 3651–3669, Jul. 2013.

[22] R. Almar, C. Blenkinsopp, L. P. Almeida, R. Cienfuegos, and P. A. Catalán, "Wave runup video motion detection using the radon transform," *Coastal Eng.*, vol. 130, pp. 46–51, Dec. 2017.

[23] T. Aagaard and J. Holm, "Digitization of wave run-up using video records," *J. Coastal Res.*, vol. 5, no. 3, pp. 547–551, 1989.

[24] R. M. C. Guedes, K. R. Bryan, G. Coco, and R. A. Holman, "The effects of tides on swash statistics on an intermediate beach," *J. Geophys. Res.*, vol. 116, no. C4, pp. 1–13, 2011.

[25] M. I. Vousdoukas et al., "The role of combined laser scanning and video techniques in monitoring wave-by-wave swash zone processes," *Coastal Eng.*, vol. 83, pp. 150–165, Jan. 2014, doi: 10.1016/j.coastaleng.2013.10.013.

[26] N. Senechal, G. Coco, K. R. Bryan, and R. A. Holman, "Wave runup during extreme storm conditions," *J. Geophys. Res., Oceans*, vol. 116, no. C7, pp. 1–13, Jul. 2011.

[27] B. G. Ruessink, S. M. Arens, M. Kuipers, and J. J. A. Donker, "Coastal dune dynamics in response to excavated foredune notches," *Aeolian Res.*, vol. 31, pp. 3–17, Apr. 2018.

[28] B. L. Bruder and K. L. Brodie, "CIRN quantitative coastal imaging toolbox," *SoftwareX*, vol. 12, Jul. 2020, Art. no. 100582.

[29] A. Ellenson, J. Simmons, G. Wilson, T. Hesser, and K. D. Splinter, "Machine learning classification of beach state from Argus imagery," *Coastal Eng. Proc.*, vol. 36, p. 37, Dec. 2020.

[30] E. B. Goldstein et al., "Labeling poststorm coastal imagery for machine learning: Measurement of interrater agreement," *Earth Space Sci.*, vol. 8, no. 9, 2021, Art. no. e2021EA001896.

[31] C. E. Blenkinsopp, M. A. Mole, I. L. Turner, and W. L. Peirson, "Measurements of the time-varying free-surface profile across the swash zone obtained using an industrial LiDAR," *Coastal Eng.*, vol. 57, nos. 11–12, pp. 1059–1065, Nov. 2010, doi: 10.1016/j.coastaleng.2010.07.001.

[32] L. P. Almeida et al., "Observations of the swash zone on a gravel beach during a storm using a laser-scanner (LiDAR)," *J. Coastal Res.*, vol. 65, pp. 636–641, Jan. 2013.

[33] L. P. Almeida, G. Masselink, P. E. Russell, and M. A. Davidson, "Observations of gravel beach dynamics during high energy wave conditions using a laser scanner," *Geomorphology*, vol. 228, pp. 15–27, Jan. 2015, doi: 10.1016/j.geomorph.2014.08.019.

[34] J. W. Fiedler, K. L. Brodie, J. E. McNinch, and R. T. Guza, "Observations of runup and energy flux on a low-slope beach with high-energy, long-period ocean swell," *Geophys. Res. Lett.*, vol. 42, no. 22, pp. 9933–9941, Nov. 2015.

[35] K. L. Brodie, B. Raubenheimer, S. Elgar, R. K. Slocum, and J. E. McNinch, "LiDAR and pressure measurements of inner-surfzone waves and setup," *J. Atmos. Ocean. Technol.*, vol. 32, no. 10, pp. 1945–1959, Oct. 2015.

[36] K. L. Brodie et al., "Continuously operating dune-mounted LiDAR system at the field research facility, a report detailing LiDAR collection, processing, evaluation, and product development," ERDC/CHL Field Res. Facility, Duck, NC, USA, Tech. Rep. AD1081467, Nov. 2017.

[37] A. O'Dea, K. L. Brodie, and P. Hartzell, "Continuous coastal monitoring with an automated terrestrial LiDAR scanner," *J. Mar. Sci. Eng.*, vol. 7, no. 2, p. 37, Feb. 2019.

[38] I. L. Turner, "Simulating the influence of groundwater seepage on sediment transported by the sweep of the swash zone across macrotidal beaches," *Mar. Geol.*, vol. 125, nos. 1–2, pp. 153–174, Jun. 1995. [Online]. Available: https://www.sciencedirect.com/science/article/pii/002532279500026U

[39] Y. Ciriano, "Field observations of swash zone infragravity motions and beach cusp evolution," *J. Geophys. Res.*, vol. 110, no. C2, pp. 1–10, 2005.

[40] C. E. Blenkinsopp, I. L. Turner, M. J. Allis, W. L. Peirson, and L. E. Garden, "Application of LiDAR technology for measurement of time-varying free-surface profiles in a laboratory wave flume," *Coastal Eng.*, vol. 68, pp. 1–5, Oct. 2012. [Online]. Available: https://linkinghub.elsevier.com/retrieve/pii/S0378383912000762

[41] I. L. Turner, P. E. Russell, and T. Butt, "Measurement of wave-by-wave bed-levels in the swash zone," *Coastal Eng.*, vol. 55, no. 12, pp. 1237–1242, Dec. 2008.

[42] M. Z. Alom et al., "The history began from AlexNet: A comprehensive survey on deep learning approaches," 2018, *arXiv:1803.01164*.

[43] N. O'Mahony et al., "Deep learning vs. traditional computer vision," in *Proc. Sci. Inf. Conf.* Cham, Switzerland: Springer, 2019, pp. 128–144.

[44] A. de Silva, I. Mori, G. Dusek, J. Davis, and A. Pang, "Automated rip current detection with region based convolutional neural networks," *Coastal Eng.*, vol. 166, Jun. 2021, Art. no. 103859.

[45] D. Buscombe and A. Ritchie, "Landscape classification with deep neural networks," *Geosciences*, vol. 8, no. 7, p. 244, Jul. 2018.

[46] D. Buscombe, R. J. Carini, S. R. Harrison, C. C. Chickadel, and J. A. Warrick, "Optical wave gauging using deep neural networks," *Coastal Eng.*, vol. 155, Jan. 2020, Art. no. 103593.

[47] C. E. Stringari, D. L. Harris, and H. E. Power, "A novel machine learning algorithm for tracking remotely sensed waves in the surf zone," *Coastal Eng.*, vol. 147, pp. 149–158, May 2019, doi: 10.1016/j.coastaleng.2019.02.002.

[48] D. Buscombe and R. J. Carini, "A data-driven approach to classifying wave breaking in infrared imagery," *Remote Sens.*, vol. 11, no. 7, p. 859, Apr. 2019. [Online]. Available: https://www.mdpi.com/2072-4292/11/7/859

[49] F. J. Sáez, P. A. Catalán, and C. Valle, "Wave-by-wave nearshore wave breaking identification using U-Net," *Coastal Eng.*, vol. 170, Dec. 2021, Art. no. 104021. [Online]. Available: https://linkinghub.elsevier.com/retrieve/pii/S037838392100168X

[50] C. E. Stringari, P. V. Guimarães, J.-F. Filipot, F. Leckler, and R. Duarte, "Deep neural networks for active wave breaking classification," *Sci. Rep.*, vol. 11, no. 1, p. 3604, Feb. 2021. [Online]. Available: https://www.nature.com/articles/s41598-021-83188-y

[51] C. E. Stringari and H. E. Power, "LiDAR observations of multimodal swash probability distributions on a dissipative beach," *Remote Sens.*, vol. 13, no. 3, p. 462, Jan. 2021. [Online]. Available: https://www.mdpi.com/2072-4292/13/3/462

[52] R. Benshila, G. Thoumyre, M. A. Najar, G. Abessolo, and R. Almar, "A deep learning approach for estimation of the nearshore bathymetry a deep learning approach for estimation of the nearshore," *J. Coastal Res.*, vol. 95, no. 1, pp. 1011–1015, 2020.

[53] A. M. Collins et al., "Bathymetric inversion and uncertainty estimation from synthetic surf-zone imagery with machine learning," *Remote Sens.*, vol. 12, no. 20, p. 3364, 2020.

[54] A. M. Collins, M. P. Geheran, T. J. Hesser, A. S. Bak, K. L. Brodie, and M. W. Farthing, "Development of a fully convolutional neural network to derive surf-zone bathymetry from close-range imagery of waves in Duck, NC," *Remote Sens.*, vol. 13, no. 23, pp. 1–17, 2021.

[55] M. Al Najar, G. Thoumyre, E. W. J. Bergsma, R. Almar, R. Benshila, and D. G. Wilson, "Satellite derived bathymetry using deep learning," *Mach. Learn.*, vol. 2021, pp. 1–24, Jul. 2021. [Online]. Available: https://link.springer.com/10.1007/s10994-021-05977-w

[56] M. A. Najar et al., "Coastal bathymetry estimation from Sentinel-2 satellite imagery: Comparing deep learning and physics-based approaches," *Remote Sens.*, vol. 14, no. 5, p. 1196, Feb. 2022. [Online]. Available: https://www.mdpi.com/2072-4292/14/5/1196

[57] T. Beuzen, J. Simmons, M. Harley, N. G. Plant, and H. F. Stockdon, "A machine learning approach for identifying dune toes on beach profile transects," in *Proc. AGU Fall Meeting Abstr.*, 2019, pp. 1–54.

[58] T. Beuzen, E. B. Goldstein, and K. D. Splinter, "Ensemble models from machine learning: An example of wave runup and coastal dune erosion," *Natural Hazards Earth Syst. Sci.*, vol. 19, no. 10, pp. 2295–2309, 2019.

[59] O. Ronneberger, P. Fischer, and T. Brox, "U-Net: Convolutional networks for biomedical image segmentation," in *Proc. Int. Conf. Med. Image Comput. Comput.-Assist. Intervent.* Cham, Switzerland: Springer, 2015, pp. 234–241.

[60] G. Wu et al., "A stacked fully convolutional networks with feature alignment framework for multi-label land-cover segmentation," *Remote Sens.*, vol. 11, no. 9, p. 1051, 2019.

[61] W. Yao, Z. Zeng, C. Lian, and H. Tang, "Pixel-wise regression using U-Net and its application on pansharpening," *Neurocomputing*, vol. 312, pp. 364–371, Oct. 2018.

[62] W. C. O'Reilly, T. H. C. Herbers, R. J. Seymour, and R. T. Guza, "A comparison of directional buoy and fixed platform measurements of Pacific swell," *J. Atmos. Ocean. Technol.*, vol. 13, no. 1, pp. 231–238, Feb. 1996.

[63] P. Rogowski et al., "Performance assessments of hurricane wave hindcasts," *J. Mar. Sci. Eng.*, vol. 9, no. 7, p. 690, 2021.